PHYSICAL REVIEW LETTERS

Rapidly Accelerating Mathieu and Weber Surface Plasmon Beams

Ana Libster-Hershko, Itai Epstein, and Ady Arie[*]

Department of Physical Electronics, Faculty of Engineering, Tel-Aviv University, Tel-Aviv 69978, Israel

We report the generation of two types of self-accelerating surface plasmon beams which are solutions of the nonparaxial Helmholtz equation in two dimensions. These beams preserve their shape while propagating along either elliptic (Mathieu beam) or parabolic (Weber beam) trajectories. We show that owing to the nonparaxial nature of the Weber beam, it maintains its shape over a much larger distance along the parabolic trajectory, with respect to the corresponding solution of the paraxial equation—the Airy beam. Dynamic control of the trajectory is realized by translating the position of the illuminating free-space beam. Finally, the ability of these beams to self-heal after blocking obstacles is demonstrated as well.

"Self-accelerating" beams, i.e., beams that maintain their shape while propagating along curved trajectories in free-space, are raising great interest in recent years [1]. The Airy wave function was the first to exhibit the above property. It was suggested in the framework of quantum mechanics by Berry and Balazs more than 30 years ago [2], as a solution to the Schrödinger equation for a free particle. However, only in 2007, optical Airy beams were suggested and observed with free-space light beams [3,4] as a solution of the paraxial Helmholtz equation, which is analogous to the Schrödinger equation. Self-accelerating free-space beams that accelerate along arbitrary convex trajectories have also been realized [5,6]. Recently, a new group of accelerating beams was introduced, i.e., half-Bessel, Mathieu, and Weber beams [7–13]. These beams are exact solutions of the nonparaxial Helmholtz equation, and therefore enable one to achieve rapid acceleration, having much sharper angles with respect to the optical axis. Self-accelerating beams usually have two additional interesting features: they are "diffraction-free"—i.e., preserve their shape while propagating, and exhibit "self-healing"—even if part of the beam is blocked by an obstacle, it returns to its original shape. While these features describe infinite energy self-accelerating beams, a finite energy beam can be obtained by truncating the long transverse tails of these beams, e.g., using an exponential or Gaussian envelope. In this case, the generated beam will exhibit these features only over finite distance. All the above mentioned beams have a highly asymmetric transverse shape, consisting of a large number of side lobes, predominantly at one side of the optical axis. The intensity of these side lobes decays as the distance from the optical axis increases. The self-acceleration property comes from constructive interference of light from these side lobes, regenerating the peak intensity lobe along a curved trajectory in space [14]. It is also important to note that the center of mass of the truncated beams propagates in a straight line, in accordance with Ehrenfest's theorem [4].

A unique feature of the Airy beam is that it maintains its shape also in a two-dimensional system, consisting of a single transverse coordinate in addition to the propagation coordinate. Therefore, it can also exist as a surface wave, such as a surface-plasmon-polariton (SPP) wave. SPPs are electromagnetic waves that are coupled to collective electron oscillations in the metal and propagate along the interface between a dielectric and a metal layer. The electric field decays exponentially normal to the dielectric metal plane, and, in addition, exhibits decay in the propagation direction. The ability to control and guide plasmonic light waves has gained a lot of interest in recent years [15,16]. On-chip technologies such as surface plasmon circuitry [17], subwavelength optical devices [18,19] and nanoscale electro-optics [20], as well as new applications in biosensing, optical trapping, and micromanipulation at the nanoscale [21] were proposed and demonstrated. Plasmonics can be used for interconnecting CMOS chips due to their ability to guide light on small wires [22], and specifically to obtain curved routing capabilities [23,24]. Indeed, plasmonic self-accelerating Airy beams were proposed [25] and experimentally demonstrated [26–29] by different research groups using various experimental tools. Plasmonic beams that propagate along arbitrary convex caustic trajectories [30] were recently demonstrated as well; however, these beams do not solve the propagation equation and do not preserve their transverse shape while propagating.

The above mentioned Mathieu and Weber beams are solutions of the two-dimensional Helmholtz equation and are therefore defined with only a single transverse coordinate and a propagation coordinate. However, up until now all the demonstrations of nonparaxial accelerating beams were done in free-space, with a broad beam (approximating a plane wave) in the third dimension. The realization of these nonparaxial accelerating beams in a two dimensional system remained an open challenge, since they need to be excited from a free-space beam, having a different wave

vector and, in addition, their transverse amplitude and phase distribution should be defined with subwavelength resolution. In this Letter, we demonstrate and examine, both numerically and experimentally, the first realization of rapidly accelerating Mathieu and Weber beams in a low-dimensional system, as they are defined and, in particular, as plasmonic surface waves.

Mathieu and Weber beams are the exact solutions of the nonparaxial two-dimensional Helmholtz equation.

$$\frac{\partial^2 A}{\partial y^2} + \frac{\partial^2 A}{\partial z^2} + k^2 A = 0, \tag{1}$$

where k is the wave vector and A is the complex amplitude. Unlike the case of free-space beams which support both TE and TM polarization [9], in the case of SPPs only TM polarization is possible. Mathieu and Weber beams differ by the coordinate systems in which they are described. The Mathieu beam is a solution of the Helmholtz equation in an elliptical coordinate system, and propagates along an elliptical trajectory. It can be mathematically expressed using

$$M(\xi, \eta) = R_m(\xi; q)[ce_m(\eta; q) - ise_m(\eta; q)], \tag{2}$$

where ξ and η are the elliptic coordinates, R_m are the radial Mathieu functions, ce_m and se_m are the even and odd angular Mathieu functions, respectively [31], m is the order of the functions, $q = h^2 k^2/4$, $h = |a^2 - b^2|^{1/2}$ is the interfocal separation, and a and b are the axes of the ellipse. The elliptic coordinates ξ and η are defined as $y = h \sinh \xi \sin \eta$ and $z = h \cosh \xi \cos \eta$. The Mathieu beam's mathematical expression can be written in the form of $M(\xi, \eta) = R(\xi)\Theta(\eta)$, where R and Θ express the solutions of the Helmholtz equation. This form allows one to separate the Helmholtz equation into two independent sections: $\Theta(\eta)$ which describes the propagation of the beam and $R(\xi)$ which describes the transverse beam's profile. In elliptic coordinates, $\Theta(\eta)$ is almost constant and by transferring the coordinate system to Cartesian, the trajectory becomes elliptic [32]. While the intensity of the beam varies along its trajectory, the lobes size and the overall shape remain constant. For the special case of circular trajectory ($a = b$)—the so-called half-Bessel beam [9]—the beam intensity distribution becomes propagation invariant [12].

The Weber beam is described by a parabolic coordinate system, and propagates along a parabolic trajectory. It can be mathematically expressed using

$$W(\eta, \xi; \gamma) = \frac{1}{2\pi}\left[\begin{array}{c}|\Gamma_1|^2 P_0(\sqrt{2k}\xi; \gamma)P_0(\sqrt{2k}\eta; -\gamma) \\ +2i|\Gamma_3|^2 P_1(\sqrt{2k}\xi; \gamma)P_1(\sqrt{2k}\eta; -\gamma)\end{array}\right], \tag{3}$$

where η and ξ are the parabolic coordinates, $\Gamma_1 \equiv \Gamma(0.25 + i\gamma/2)$, $\Gamma_3 \equiv \Gamma(0.75 + i\gamma/2)$, γ is the dimensionless parabolic momentum, and P are the parabolic cylinder functions [31]. It is also possible to write these functions in terms of the Kummer confluent hypergeometric function $_1F_1$ [31], which is the manner we have taken. The parabolic coordinates η and ξ are defined according to the relation $y + iz = (\eta + i\xi)^2/2$. Similar to Mathieu, the Weber beam's mathematical expression is in the form of $W(\xi, \eta) = \Phi(\xi)\vartheta(\eta)$, where Φ and ϑ express the solutions of the Helmholtz equation. $\Phi(\xi)$ describes the transverse beam's profile and $\vartheta(\eta)$ describes the propagation of the beam. The dependence of the beam on the propagation coordinate η [7] can be approximated by $\propto[1/(\eta^2 k/2\gamma + 1)]^{1/4}$, since typically $\eta \ll 1$ the beam can be considered as diffraction-free in the parabolic coordinate system—it is nearly independent of the propagation coordinate and maintains its transverse shape. By transferring the parabolic coordinates to Cartesian coordinates system, the trajectory of the beam becomes parabolic, since $\vartheta(\eta)$ is nearly constant [32].

The acceleration trajectories of both beams can be expressed mathematically. For the Mathieu beam the elliptical trajectory is defined by $y = \pm b\sqrt{1 - (z/a)^2}$, where a and b are the major and minor axes of the ellipse, respectively, and for the Weber beam the parabolic trajectory is defined by $y = kz^2/(4\gamma)$, where γ is the dimensionless parabolic momentum [7]. The angle of every beam can be represented by the derivative of the trajectory of this beam by z. For the Weber beam the angle is $dy/dz = kz/2\gamma$ and for the Mathieu beam the angle is $dy/dz = \mp bz/(a^2\sqrt{1 - (z/a)^2})$. For the Airy beam the trajectory is $y = z^2/(4k^2x_0^3)$, and therefore the angle is $dy/dz = z/(2k^2x_0^3)$. The size of x_0 should be considerably larger than the wavelength in order for the Airy beam to satisfy the paraxial approximation. In contrast to that, the Weber and Mathieu beams do not possess this limitation, which enables the beams to propagate with larger angles.

In order to generate plasmonic Mathieu and Weber beams, it is required to couple a free-space illuminating beam into the SPP beam and also to define its phase and amplitude distribution. This was achieved using our recently developed method for designing plasmonic holograms for the near-field [33]. In this method, the phase mismatch between the wave vectors of the free-space beam and the plasmonic beam is matched by the reciprocal vector of the near-field hologram in the direction of propagation, and therefore couples to the SPP. This plasmonic hologram also encodes the transverse phase $\phi(z, y)$ and amplitude $A(z, y)$ of the near field of the desired Mathieu and Weber beams. The plasmonic binary hologram was encoded according to [33,34]

$$t(z, y) = \frac{h_0}{2}\left\{1 + \text{sgn}\left[\cos\left(\frac{2\pi}{\Lambda}z + \phi(z, y)\right) - \cos(\pi q)\right]\right\}, \tag{4}$$
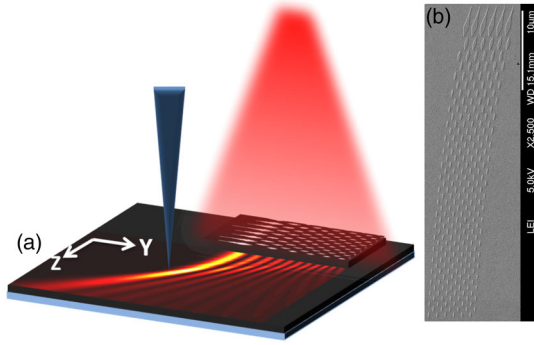
FIG. 1 (color online). (a) The experimental setup.(b) SEM image of the plasmonic hologram which generated the plasmonic Weber beam starting from $z = -15\mu m$ with $\gamma = 120$.

where Λ is the modulation period, $q = \sin^{-1}[A(z,y)]/\pi$, and h_0 is the ridge height.

The SPPs were generated between a silver layer and air. The thickness of the silver layer was 200 nm and it was evaporated on top of a glass substrate. The silver layer was coated with polymethyl methacrylate resist and the plasmonic hologram was written using electron beam lithography. Then, the resist was developed and another layer of silver was evaporated. Finally, a liftoff process was performed to remove the resist and the metal layer that covered it. The thickness of the silver plasmonic hologram was set to 50 nm. For the permittivity of the silver metal we used $\varepsilon_m = -58.04 + 0.6089i$ and $\varepsilon_d = 1$ for the permittivity of the air. The decay length perpendicular to the propagation direction is 11 nm in the metal and 640 nm in air. This is an inherent property of surface plasmons and therefore the realization of a self-accelerating beam is not affected by this transverse decay. The decay in the propagation direction is 0.9 mm, and since we are measuring the beam profile at much shorter distances, this decay is negligible. The experimental setup is presented in Fig. 1(a)—the plasmonic hologram is illuminated by a laser beam at wavelength of 1.064 μm, and the intensity distribution of the generated SPPs between the silver and air was measured using a near-field-scanning-optical microscope (NSOM—Nanonics MultiView 2000). A SEM image of the plasmonic hologram which generated the plasmonic Weber beam is presented in Fig. 1(b). This mask was designed to generate a Weber beam with $\gamma = 120$ by exciting forty lobes. The main lobe width was ~3 μm and the last lobe size was ~0.5 μm.

The presented numerical simulations of the evaluation and propagation of the self-accelerating SPPs were performed based on the 2D Green function of the Helmholtz equation. Figure 2 shows the comparison between the numerical simulations and the measured NSOM results for a plasmonic Mathieu beam accelerating from $z = 0$ μm [Figs. 2(a) and 2(b)], a plasmonic circular Mathieu beam starting from $z = -15$ μm [Figs. 2(c) and 2(d)], and
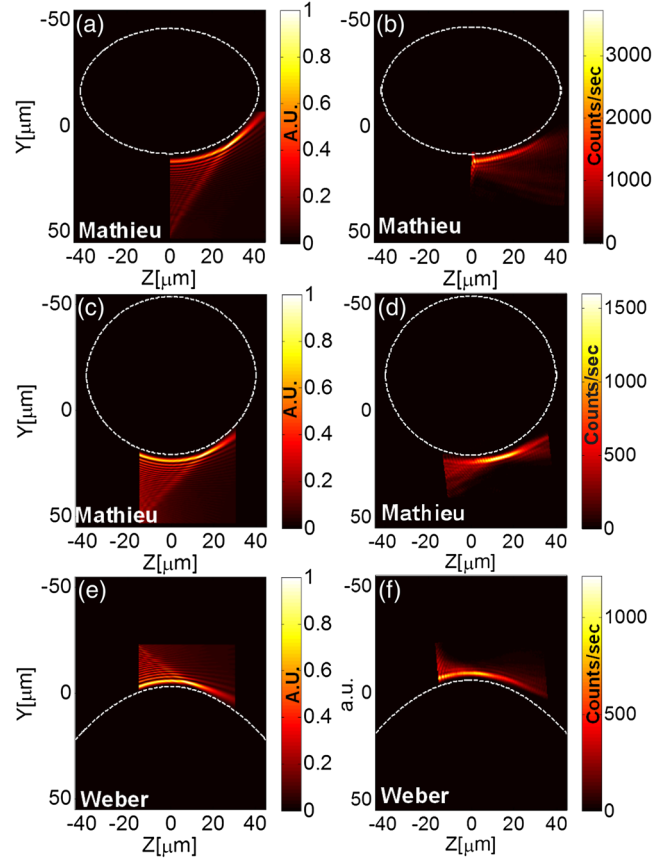
FIG. 2 (color online). Comparison between measured and simulated self-accelerating beams intensity distribution. Numerical simulations (a),(c),(e) and NSOM measurements (b),(d),(f) of a Mathieu beam starting from $z = 0$ μm, circular Mathieu starting at $z = -15$ μm and Weber beam starting from $z = -15$ μm with $\gamma = 120$, respectively. The dashed white line represents the analytical trajectory of the beam.

plasmonic Weber beams accelerating from $z = -15$ μm [Figs. 2(e) and 2(f)]. It is clearly seen that there is good agreement between the simulations and the experimental results. It is also seen that all the measured beams are propagating along the designed acceleration trajectory (white dashed lines). As expected from the inherent finite size of the masks, the beams deviate from the analytical trajectory at a certain point. This deviation occurs sooner when sharp bends are sought as expected from finite energy beams. We note that the smaller lobes are excited with lower efficiency in the experiment, causing a faster deviation from the target curve. This is caused by the Gaussian distribution of the illuminating free-space beam, whereas our design assumed plane-wave illumination. We also note that the vast freedom of this method allows one to arbitrarily choose the starting z value of the accelerating beam, being limited mainly by the fabrication process, as the hologram's features get smaller. The angles at $z = 30$ μm for the beams presented in Fig. 2 are 36.6° for Weber
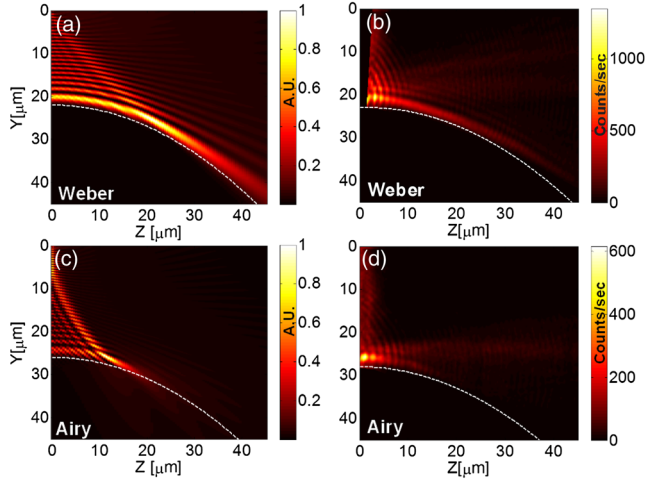
FIG. 3 (color online). Comparison between measured and simulated Airy and Weber beams. Numerical simulations (a), (c) and NSOM measurements (b),(d) of the intensity distribution Weber beam with $\gamma = 120$ and equivalent Airy beams. The dashed white line represents the analytical trajectory of the beam.

FIG. 4 (color online). Dynamic control of the direction of Weber beams. NSOM intensity distribution measurements (a), (b),(c) of Weber beam with $\gamma = 120$ illuminated with the top, middle, and bottom part of the Gaussian free space beam, respectively. The dashed white line represents the analytical trajectory of the beam.

beam with $\gamma = 120$, 48.1° for circular Mathieu beam with $a = b = 40\ \mu$m, and 37.2° for Mathieu beam with $a = 42$ and $b = 32\ \mu$m. In comparison to the beams from Fig. 2, the angle at $z = 30\ \mu$m for the Airy beam, even with $x_0 = \lambda$, is 19.8°. Next, we compare the rapid acceleration of the nonparaxial Weber beam with that of the paraxial Airy beams. As both beams accelerate along a parabolic trajectory, we defined an Airy beam $\text{Ai}(x/x_0)$ with a characteristic size of $x_0 = 0.82\ \mu$m and a corresponding Weber beam with a parabolic momentum $\gamma = 120$, so that both beams have the same acceleration coefficient of $1.24 \times 10^4 [1/\text{m}]$. The simulation and measurement results are presented in Fig. 3 and it can be seen that whereas the Airy beam deviates from this trajectory after only a few microns of propagation and then breaks into multiple lobes [35], the Weber beam preserves its shape and propagates over a distance of ∼40 μm along the target parabolic trajectory. This demonstration emphasizes the advantages of the nonparaxial self-accelerating beams over the paraxial-limited beams that were realized before. In the Supplemental Material [32] we show the simulation results of a systematic comparison between the Airy and Weber beams as a function of the acceleration coefficient.

By controlling the illumination angle of the input free-space beam, it is possible to dynamically control the direction of propagation of the launched self-accelerating beams [36,37]. Here we realize this by illuminating the plasmonic hologram with the tail of the free-space Gaussian beam. By doing so, a tilted phase is being added to the hologram and the beam's direction can be changed. Figure 4 shows the results of such measurements under three different illumination states. This allows flexible
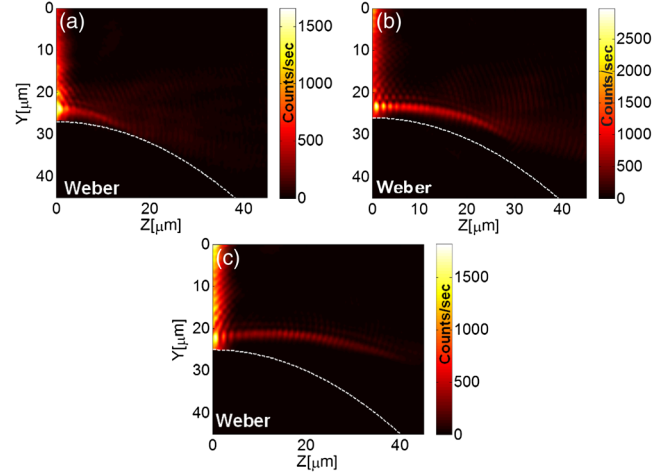
routing of the beam energy to different locations on the surface.

Finally, we examine the self-healing property of the generated beams. We note that this unique property is also typical for other shape preserving beams such as Bessel, Airy beams, and Cosine-Gauss beams [38]. We therefore fabricated a sample in which an obstacle that blocked the main lobe of the beam was added, by milling a small rectangular region in the silver layer using a focused-ion-beam. In this region only the dielectric substrate was left, thereby blocking the plasmonic beam at this spot. As the beam propagates, the main lobe is being reconstructed, therefore exhibiting the expected self-healing property. The results are presented in Fig. 5 for both plasmonic Mathieu and Weber beams. Since the purpose of these measurements was to show the phenomenon and not to compare between the self-healing capabilities of the beams, the blocking obstacles in the samples differed by their size and
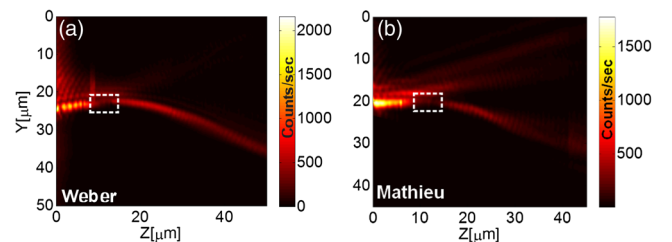
FIG. 5 (color online). Demonstration of the self-healing property of plasmonic Weber (a) and Mathieu (b) beams, by measuring their intensity distribution before and after a blocking obstacle. The white dashed rectangle depicts the location of the obstacle.

location, thereby explaining the observed difference in the healing dynamics.

In conclusion, in this work we presented the first realization of rapidly self-accelerating Weber and Mathieu plasmonic surface waves. This realization can enable new possibilities in photonics and plasmonics, which are no longer limited by the paraxial approximation. It is worth mentioning that Mathieu and Weber beams have been already used for optical trapping and micromanipulation in 3D [13], and therefore our demonstration may enable new ways for particle manipulation near a metallic surface [21]. We also note that owing to the wave nature of the beams, these beams can be also realized as other surface waves, such as acoustic waves [39,40], ground radio waves, or surface fluid waves, and in other types of low-dimensional systems such as dielectric optical waveguides, graphene-based systems, etc. These waves are expected to be self-healing, shape-preserving, and self-accelerating along nonparaxial trajectories.

---

*Corresponding author.
ady@post.tau.ac.il

[1] Y. Hu, G. A. Siviloglou, P. Zhang, N. K. Efremidis, D. N. Christodoulides, and Z. Chen, *Self-Accelerating Airy Beams: Generation, Control, and Applications* (Springer, New York, 2012), p. 1.

[2] M. V. Berry, Am. J. Phys. **47**, 264 (1979).

[3] G. A. Siviloglou and D. N. Christodoulides, Opt. Lett. **32**, 979 (2007).

[4] G. A. Siviloglou, J. Broky, A. Dogariu, and D. N. Christodoulides, Phys. Rev. Lett. **99**, 213901 (2007).

[5] L. Froehly, F. Courvoisier, A. Mathis, M. Jacquot, L. Furfaro, R. Giust, P. A. Lacourt, and J. M. Dudley, Opt. Express **19**, 16455 (2011).

[6] E. Greenfield, M. Segev, W. Walasik, and O. Raz, Phys. Rev. Lett. **106**, 213902 (2011).

[7] M. A. Bandres and B. M. Rodríguez-Lara, New J. Phys. **15**, 013054 (2013).

[8] P. Zhang, Y. Hu, T. Li, D. Cannan, X. Yin, R. Morandotti, Z. Chen, and X. Zhang, Phys. Rev. Lett. **109**, 193901 (2012).

[9] I. Kaminer, R. Bekenstein, J. Nemirovsky, and M. Segev, Phys. Rev. Lett. **108**, 163901 (2012).

[10] C. Alpmann, R. Bowman, M. Woerdemann, M. Padgett, and C. Denz, Opt. Express **18**, 26084 (2010).

[11] P. Rose, M. Boguslawski, and C. Denz, New J. Phys. **14**, 033018 (2012).

[12] P. Aleahmad, M.-A. Miri, M. S. Mills, I. Kaminer, M. Segev, and D. N. Christodoulides, Phys. Rev. Lett. **109**, 203902 (2012).

[13] C. Alpmann, M. Boguslawski, P. Rose, M. Wördemann, and C. Denz, in *Complex Light Optical Forces VI*, edited by E. J. Galvez and D. L. Andrews, J. Glückstad, and M. S. Soskin, SPIE Proceedings Vol. 8274 (SPIE-International Society for Optical Engineering, Bellingham, WA, 2012), p. 82740R.

[14] Y. Kaganovsky and E. Heyman, Opt. Express **18**, 8440 (2010).

[15] H. A. Atwater, Sci. Am. **296**, 56 (2007).

[16] M. L. Brongersma and V. M. Shalaev, Science **328**, 440 (2010).

[17] T. W. Ebbesen, C. Genet, and S. I. Bozhevolnyi, Phys. Today **61**, No. 5, 44 (2008).

[18] W. L. Barnes, A. Dereux, and T. W. Ebbesen, Nature (London) **424**, 824 (2003).

[19] D. K. Gramotnev and S. I. Bozhevolnyi, Nat. Photonics **4**, 83 (2010).

[20] E. Ozbay, Science **311**, 189 (2006).

[21] M. L. Juan, M. Righini, and R. Quidant, Nat. Photonics **5**, 349 (2011).

[22] J. Leuthold, C. Hoessbacher, S. Muehlbrandt, A. Melikyan, M. Kohl, C. Koos, W. Freude, V. Dolores-Calzadilla, M. Smit, I. Suarez, J. Martínez-Pastor, E. P. Fitrakis, and I. Tomkos, Opt. Photonics News **24**, 28 (2013).

[23] P. Berini and J. Lu, Opt. Express **14**, 2365 (2006).

[24] J. T. Kim, S. Park, J. J. Ju, S. Lee, and S. Kim, Opt. Express **18**, 24213 (2010).

[25] A. Salandrino and D. N. Christodoulides, Opt. Lett. **35**, 2082 (2010).

[26] A. Minovich, A. E. Klein, N. Janunts, T. Pertsch, D. N. Neshev, and Y. S. Kivshar, Phys. Rev. Lett. **107**, 116802 (2011).

[27] L. Li, T. Li, S. M. Wang, C. Zhang, and S. N. Zhu, Phys. Rev. Lett. **107**, 126804 (2011).

[28] P. Zhang, S. Wang, Y. Liu, X. Yin, C. Lu, Z. Chen, and X. Zhang, Opt. Lett. **36**, 3191 (2011).

[29] A. E. Minovich, A. E. Klein, D. N. Neshev, T. Pertsch, Y. S. Kivshar, and D. N. Christodoulides, Laser Photonics Rev. **8**, 221 (2014).

[30] I. Epstein and A. Arie, Phys. Rev. Lett. **112**, 023903 (2014).

[31] M. Abramowitz and I. A. Stegun, *Handbook of Mathematical* (Dover, New York, 1972).

[32] See Supplemental Material at http://link.aps.org/supplemental/10.1103/PhysRevLett.113.123902 for for comparison between Weber and Airy beams, analysis of self acceleration and plasmon dependence on X direction.

[33] I. Epstein, Y. Lilach, and A. Arie, J. Opt. Soc. Am. B **31**, 1642 (2014).

[34] W. H. Lee, Appl. Opt. **18**, 3661 (1979).

[35] A. V. Novitsky and D. V. Novitsky, Opt. Lett. **34**, 3430 (2009).

[36] I. Epstein and A. Arie, Opt. Lett. **39**, 3165 (2014).

[37] G. A. Siviloglou, J. Broky, A. Dogariu, and D. N. Christodoulides, Opt. Lett. **33**, 207 (2008).

[38] J. Lin, J. Dellinger, P. Genevet, B. Cluzel, F. de Fornel, and F. Capasso, Phys. Rev. Lett. **109**, 093904 (2012).

[39] Y. Zhou, M.-H. Lu, L. Feng, X. Ni, Y.-F. Chen, Y.-Y. Zhu, S.-N. Zhu, and N.-B. Ming, Phys. Rev. Lett. **104**, 164301 (2010).

[40] B. Diaconescu, K. Pohl, L. Vattuone, L. Savio, P. Hofmann, V. M. Silkin, J. M. Pitarke, E. V. Chulkov, P. M. Echenique, D. Farías, and M. Rocca, Nature (London) **448**, 57 (2007).